RESEARCH ARTICLE

NANO · MICRO small
www.small-journal.com

In Situ Formed Continuous and Dense Inorganic Borate-Based SEI for High-Performance Li-Metal Batteries

Yuying Liu, Tao Huang, Zhencheng Huang, Weiyuan Huang, Jing Chen, Hao Jia, Xuanlong He, Weibin Chen, Haoran Wei, Liewu Li, Xiangzhong Ren, Xiaoping Ouyang, Jianhong Liu, Shenghua Ye, Xuming Yang,* Feng Pan,* Qianling Zhang,* and Jiangtao Hu**

The practical application of lithium metal batteries (LMBs) is largely hindered by the notorious lithium dendrite growth, low cycle efficiency associated with insufficient electrode–electrolyte interphase dynamics, and electrolyte combustion. Here, an advanced electrolyte using a combination of three kinds of salts dissolved in carbonate-based solvents is developed. The salt anions dominate a primary solvation sheath, resulting in weak interaction between Li^+ and the solvents, as well as the in situ formation of an inorganic-rich bilayer solid electrolyte interface (SEI). The designed electrolyte enables high cycle stability in LMBs with a high-loading NMC cathode (approximately 20 mg cm^{-2}), exhibiting 89.89% capacity retention after 200 cycles with the cutoff voltage of 4.5 V. Cryo-TEM characterization and density-functional theory (DFT) calculations reveal that the borate-based bilayer SEI, characterized by an exceptional dense structure, effectively suppresses lithium dendrite growth, and certify the crucial role of inorganic component continuity and density within the SEI, which surpasses the absorption and migration energy barrier in terms of significance. This profound understanding of SEI structure holds great potential for advancing the development of high-stable LMBs and can be expanded to other battery system.

1. Introduction

Lithium-ion batteries (LIBs) are a major driver in the new energy era, and have found extensive applications in portable electronic devices, aerospace, and hybrid or plug-in electric vehicles since Sony launched the first commercial LIB in 1991.[1] In the pursuit of higher energy density in next-generation batteries, lithium metal anode emerges as a promising candidate due to its remarkable ultrahigh capacity (3860 mAh g^{-1}) and exceptionally low potential (-3.040 V vs standard hydrogen electrode).[2–4] However, the uncontrollable growth of dendrites in lithium metal batteries (LMBs) raises significant safety concerns. The high Fermi energy level of lithium metal triggers irreversible and continuous reactions with the electrolyte, leading to self-depletion, increased interfacial resistance and limited cycling life.[5,6] These issues during electrochemical processes will become severer under high areal capacity and lean-electrolyte conditions. In order to solve the above problems, researchers have modulated the lithium deposition behavior by optimizing electrolyte components,[7,8] developing solid-state electrolytes,[9] constructing artificial SEI films,[10,11] and designing 3D lithium deposition frameworks,[12,13] among other strategies. Among them, the research and development of electrolyte system is crucial to improve the performance of lithium metal anodes.[14]

Y. Liu, Z. Huang, X. He, W. Chen, H. Wei, L. Li, X. Ren, X. Ouyang, J. Liu, S. Ye, X. Yang, Q. Zhang, J. Hu
Graphene Composite Research Center
College of Chemistry and Environmental Engineering
Shenzhen University
Shenzhen 518060, China
E-mail: yeshh@szu.edu.cn; yangxm@szu.edu.cn; zhql@szu.edu.cn; hujt@szu.edu.cn

T. Huang
College of Energy Engineering
Zhejiang University
Hangzhou, Zhejiang 310027, China

The ORCID identification number(s) for the author(s) of this article can be found under https://doi.org/10.1002/smll.202406400

DOI: 10.1002/smll.202406400

W. Huang, F. Pan
School of Advanced Materials Shenzhen Graduate School
Peking University
Shenzhen 518060, China
E-mail: panfeng@pkusz.edu.cn

J. Chen, X. Ouyang
School of Materials Science and Engineering
Xiangtan University
Xiangtan 411105, China

H. Jia
School of Chemical Engineering and Technology
Sun Yat-Sen University
Zhuhai, Guangdong Province 519082, China

J. Liu
Shenzhen Eigen-Equation Graphene Technology Co. Ltd
Shenzhen 518000, China

Currently, solutions to improve the stability of lithium anodes include localized high-concentration electrolyte,[15–17] perfluoro-electrolyte[18–20] and high-concentration electrolyte[21–24] design. Localized high-concentration electrolyte can achieve uniform deposition of lithium ions on the anode side of lithium metal and ultra-high cycling stability, but the diluent has a low boiling point and is easy to be vaporized, and there are safety risks. Perfluoro-electrolyte can effectively improve the cycle stability of lithium metal batteries, but further evaluation is needed in terms of safety. High-concentration electrolytes have a unique solvent sheath structure that binds solvents and anions in the electrolyte, reducing the interfacial activity of the electrolyte and improving the stability of the battery system. Recently, Dahn and co-workers reported a high-concentration electrolyte that extended the life of anode-free batteries to 200 cycles.[25] Yamada's team conducted a year-long test (over 1000 cycles) on graphite||Li and hard carbon||Na batteries using high-concentration electrolytes, resulting in almost negligible capacity degradation.[26] A carbonate solvent-based dual-salt high-concentration electrolyte system developed by Wang et al.[27] was utilized, presenting very high Coulombic efficiency in Li||Cu batteries. Numbers of studies have demonstrated that the preferential decomposition of anions on lithium metal anodes leads to the formation of inorganic component-rich SEI that significantly enhances battery performance.[28–31] Therefore, it is of great significance to explore how the concept of high-concentration electrolytes can be employed to achieve the preferential decomposition of anions and improve the stability of lithium metal anode.

Enhanced interactions between the organic solvent and the cations or anions in the lithium salts due to increased salt concentration and types can lead to the formation of more inorganic-rich SEI layers. Here, we have developed a stable and fire-retardant concentrated electrolyte, named Tri-salts, which consists of 4 M lithium hexafluorophosphate ($LiPF_6$), lithium tetrafluoroborate ($LiBF_4$) and lithium difluoroborate (LiDFOB) dissolved in a mixture of dimethyl carbonate (DMC), ethyl carbonate (EC) and methyl ethyl carbonate (EMC). Our findings reveal that the designed Tri-salts electrolyte facilitates the in situ formation of a dense bilayer SEI rich in borates. This SEI layer effectively suppresses the growth of lithium dendrites, promotes homogeneous lithium deposition morphology, and enables LMBs with high areal capacity (approximately 4 mAh cm^{-2} of NMC83) to exhibit an impressive capacity retention rate of 89.89% after 200 cycles.

Cryo-TEM and DFT calculations validate that the compact structure of the inorganic component during the SEI formation process plays a crucial role in determining the Li^+ deposition behavior. Considering the significant influence exerted by the continuity and dense of the inorganic components in SEI, this approach provides a novel strategy for advancing high energy density LMBs.

2. Results and Discussion

2.1. Electrolyte Solvation Structure

The solvation structures of the solvents and prepared electrolytes were analyzed using Raman spectroscopy. The results of DMC, EC, EMC, Dual-salts-1, Dual-salts-2, and Tri-salts are shown in Figure 2a. Pure EC shows a strong band at 969 cm^{-1}, and pure EMC displays two absorption bands at 875 and 932 cm^{-1}. The peak at 740 cm^{-1} originates from PF_6^- coordinated to Li^+,[32,33] and the peak at 715 cm^{-1} comes from the vibrational peak of B—F,[34–36] combined with calculations, indicating that the $BF4^-$ and $DFOB^-$ were successfully incorporated into the solvated sheath in Tri-salts. Apparently, compared with the dual-salt electrolytes, DMC has strong interactions with Li^+ in Tri-salts and more DMC solvent molecules enter into the solvated sheath which is conducive to the realization of the flame-retardant property of the electrolyte. Furthermore, the self-extinguishing times (SET) were collected to evaluate the flammability of the prepared electrolytes.[37,38] As shown in Figure S1 (Supporting Information), E268 is highly flammable with a SET value of 44 s, Dual-salts-1 is 35 s and Dual-salts-2 is 28 s. As to Tri-salts, it exhibits a good flame retardancy, which means the flammable solvents were almost entering into the solvation sheath.

The evolution of the solvation structure was further investigated by molecular dynamics simulations. The snapshots (Figure S2, Supporting Information) and radial distribution functions (RDFs) between E268 and Tri-salts were compared (**Figure 1b,c**). For E268, the peaks of Li—O (EC) and Li—O (EMC) are displayed at ≈2.0 Å, whereas the peak of Li—P (PF_6^-) is much weaker, suggesting that the inner solvation sheath mainly contains EC and EMC, with only a small number of anions and solvent molecules coordinated to a single Li^+ to form CIPs. The coordination numbers of EC and EMC in E268 are 2.46 and 2.38, which further confirms that the first solvated sheath layer of E268 gathers more solvent molecules (Figure 1d). As to Tri-salts, the coordination number of EC, EMC, DMC, PF_6^-, $DFOB^-$, and BF_4^- are 0.79, 0.13, 1.76, 0.55, 0.76 and 0.70, respectively, which indicates that more anions are crowed in the primary solvation sheath (Figure 1e).

The high voltage stability of E268 and Tri-salts was examined by linear sweep voltammetry (LSV).[30,39] As shown in Figure 1f, below 5.1 V, the oxidation current of the cell with addition of LiDFOB is much larger than that of E268, implying that the oxidation of the Tri-salts electrolyte starts before E268. Interestingly, when the voltage rises to 5.1 V, the oxidation current of the E268 cell increases sharply and far exceeds that of the Tri-salts electrolyte, which indicates that the addition of LiDFOB can make the electrolyte more stable.

2.2. Electrochemical Performance

The superiority of Tri-salts was characterized by the galvanostatic cycling using Li||Li symmetric cells at 0.5 mA cm^{-2}. As depicted in **Figure 2a**, after 180 h, the polarization voltage of Li||Li cells with E268 increases rapidly due to the side reactions and the cell impedance increases dramatically, whereas the cell employing Tri-salts exhibits an extended lithium plating/stripping cycle life of up to 600 h. High mass-loading cathodes (approximately 4 mAh cm^{-1}) were adopted and tested using Li metal anodes (thickness of 450 μm) in the six different electrolytes (Figure 2b, Figure S3 and Table S1, Supporting Information). Impressive cycling performance was achieved in Tri-salts, with a high-capacity retention of 187 mAh g^{-1} (94.49%) after 100 cycles. In contrast, the Li||NCM83 batteries tested in E268 and Dual-salts-1 showed fast capacity fading, with only 4.67% and 7.24%

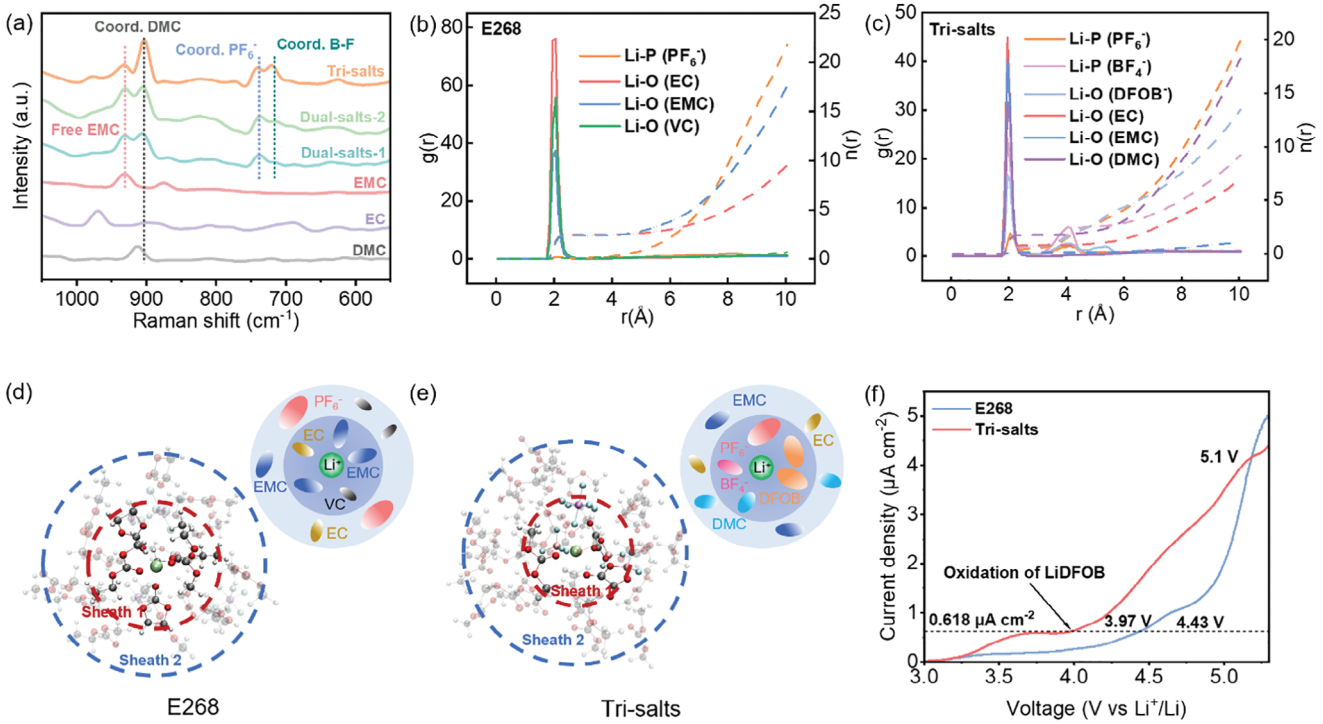

Figure 1. Characterization of the Li^+ solvation structures of the designed electrolytes. a) Raman spectra of electrolytes and solvents. b,c) RDFs $g(r)$ (solid line on left-hand axis) and running coordination number $n(r)$ (dashed line on right-hand axis) for Li—P (PF_6^-), Li—P (BF_4^-), Li—O (EC), Li—O (EMC), Li—O (VC), Li—O (DMC), and Li—O ($DFOB^-$) pairs in b) E268 and c) Tri-salts. The solvation structure of the cations in d) E268 and e) Tri-salts. f) LSV results recorded at stainless-steel plate||Li coin cells in the E268 electrolyte and Tri-salts electrolytes.

capacity retentions, respectively. After 30 cycles, the E268 and Dual-salts-1 batteries showed a large capacity degradation, which can be attributed to the accelerated interfacial reaction and the consequent consumption of electrolyte. As to the Dual-salts-2 battery, it exhibits a high-capacity retention during the first 100 cycles (Figure S3, Supporting Information). Whatmore it is well known that the Li dendrite growth and electrochemical stabilities of electrolytes have a strong impact on the CE and cycle life of LMBs. Figure S3 (Supporting Information) demonstrates the CE of Li||NMC LMBs with differently electrolytes. The CE in Tri-salts is relatively lower than that in E268 (82.53% vs 87.33%). However, once a protective interphase layer is established, it contributes to enhanced cycle stability. During the first 100 cycles, it is obvious that the CE in E268 was the lowest among the six kinds of electrolytes, and the average CE in Tri-salts is higher than that in E268 (90.85%). Moreover, the voltage decay was effectively suppressed in Tri-salts (Figure 2c and Figure S4, Supporting Information), which is consistent with its high-capacity retention rate during the long-term cycling. When lower the charge current density to 0.1C, the Tri-salts batteries could maintain 200 stable cycles with a capacity retention rate of 89.89% (Figure 2d). In addition, at high temperature (45 °C), the capacity retentions of Tri-salt based and E268 based cells are 91.08% and 15.73% after 40 cycles (Figure 2e).

For an in-depth analysis of the reasons for the superior performance of Tri-salts. The viscosities of the electrolytes were determined using a MSK-SFM-VT viscometer at 28 °C. The ionic conductivities of the electrolytes were measured by assembling symmetric stainless-steel cells. The results are shown in Tables S2 and S3 (Supporting Information), and as expected Tri-salts have the smallest ionic conductivity due to their high viscosity. Electrochemical impedance spectroscopy (EIS) tests were then performed on batteries with four electrolytes (Figure S5, Supporting Information). It can be clearly seen that as cycling proceeds the SEI resistance in Tri-salts decreases significantly compared to E268, indicating that it is easier to generate stable SEI in Tri-salts, preventing the growth of lithium dendrites, thus realizing the improvement of cycling stability. Solution impedance of the four electrolytes can be obtained from Figure S5 (Supporting Information), although solution resistance increases in all of them after cycling, but the addition of LiDFOB, the solution resistance of Dual-salts-2 and Tri-salts is obviously slower than the other two electrolytes. In addition, The Tafel plot (Figure S6, Supporting Information) showed that the symmetric cell has a significantly higher exchange current density (7.14 mA cm^{-2}) in Tri-salts than in E268 (2.09 mA cm^{-2}), Dual-salts-1 (4.32 mA cm^{-2}) and Dual-salts-2 (6.97 mA cm^{-2}), also indicating faster kinetics of Li plating in the Tri-salts electrolyte.

2.3. SEI Characterization

The lithium nucleation and deposition behavior in different electrolytes were performed in Li||Cu cells (Figure S7, Supporting Information). A large number of needle-like lithium dendrites are generated in E268, however, in Tri-salts, the lithium deposition morphology appears to be compact and characterized by particles. Then, the morphologies of the lithium metal anodes

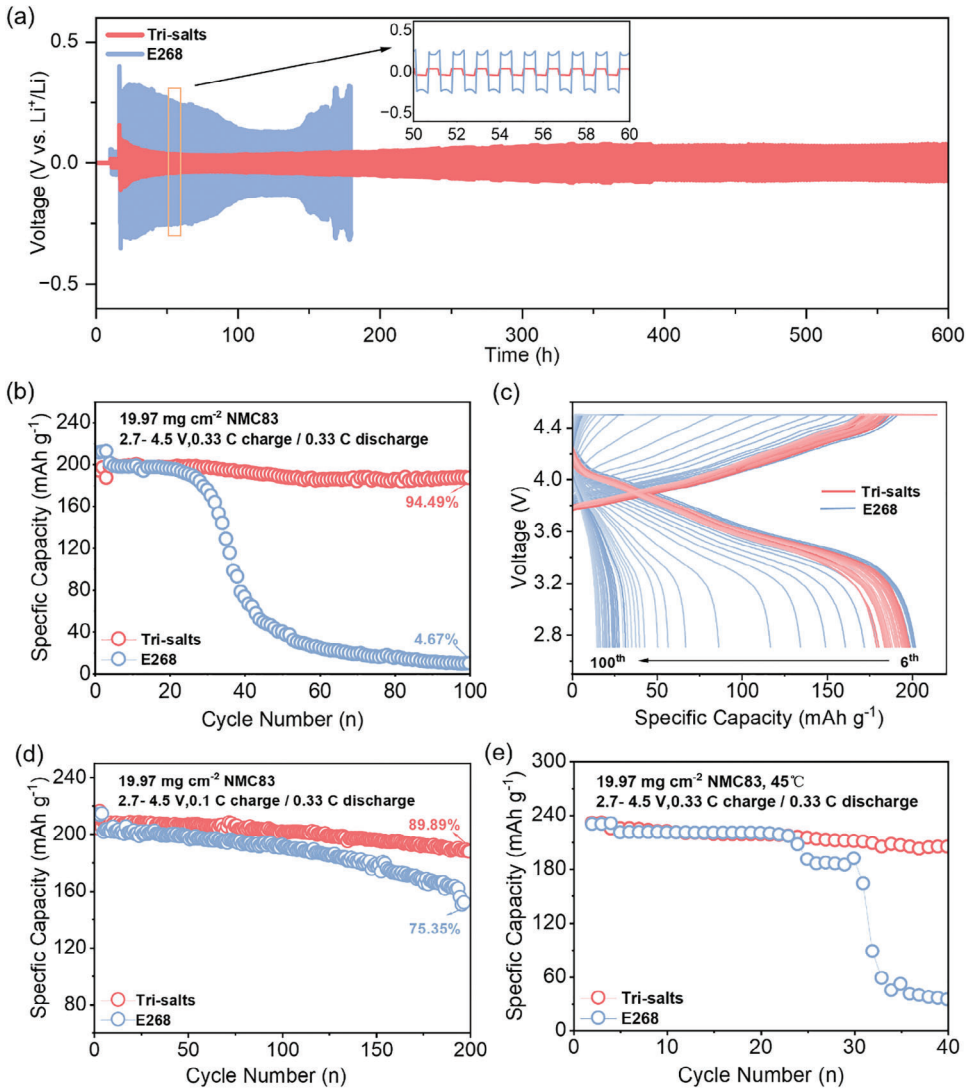

Figure 2. Electrochemical performance in different electrolytes. a) Galvanostatic cycling performance of Li||Li symmetric cells at 0.5 mA cm^{-2}. b) Cycling stability at 0.33 C charge/discharge rates. c) Corresponding charge/discharge profiles from the 6^{th} to 100^{th} cycle in E268 and Tri-salts. d) Cycling stability at 0.1C charge and 0.33C discharge rates. e) Cycling stability at 0.33 C charge/discharge rates in 45 °C.

after 100 cycles in Li||NMC83 were characterized (**Figures** 3a,b and S8a-d, Supporting Information). Elongated needle-like structures were observed in E268 and Dual-salts-1 (Figure 3a and Figure S6a, Supporting Information), indicating the occurrence of severe lithium dendrite growth with a highly porous structure. The Tri-salts and Dual-salts-2 electrolytes yielded dendrite-free and finely deposited particles, demonstrating excellent consistency with enhanced cycle stability (Figure 3b and Figure S8c,d, Supporting Information). Furthermore, the thicknesses of the corrosion layer of the lithium metal in different electrolytes were collected, and the lithium metal tested in Tri-salts electrolyte performed the minimized reaction thickness, which is around 390 µm (Figure S8h, Supporting Information).

Cryo-TEM was utilized to characterize the morphology of the deposited lithium and the SEI layer on the surface of lithium metal anode. Figure 3c–f further confirms the difference of the deposited lithium, which is consistent to the SEM images. The SEI layer formed in the cell with E268 electrolyte is basically amorphous with some Li_2O distributed inside (Figure 3g,h and Figure S9, Supporting Information). However, the cell with the Tri-salts electrolyte formed a uniform and dense double-layer SEI layer with a thickness of 8.5 nm on the lithium metal surface, and it can be seen from the high-resolution images that the SEI appeared to be clearly stratified, with a large-scale crystalline substance present in the surface layer, and a predominantly amorphous morphology in the inner layer (Figure 3k and Figure S10a-d, Supporting Information). From the high-resolution images and corresponding fast Fourier transform (FFT) patterns, the measured lattice stripe spacing values are 2.66, 2.72, and 3.05 Å, which can be matched with the standard lattice spacing of Li_2O, Li_3BO_3 and $Li_4B_2O_5$ respectively (Figure 3l and Figure S10e,f, Supporting Information).[40–42] The electron energy loss spectroscopy (EELS) of the SEI layers obtained from E268 and Tri-salts batteries were demonstrated in Figure 3i,j,n,m.

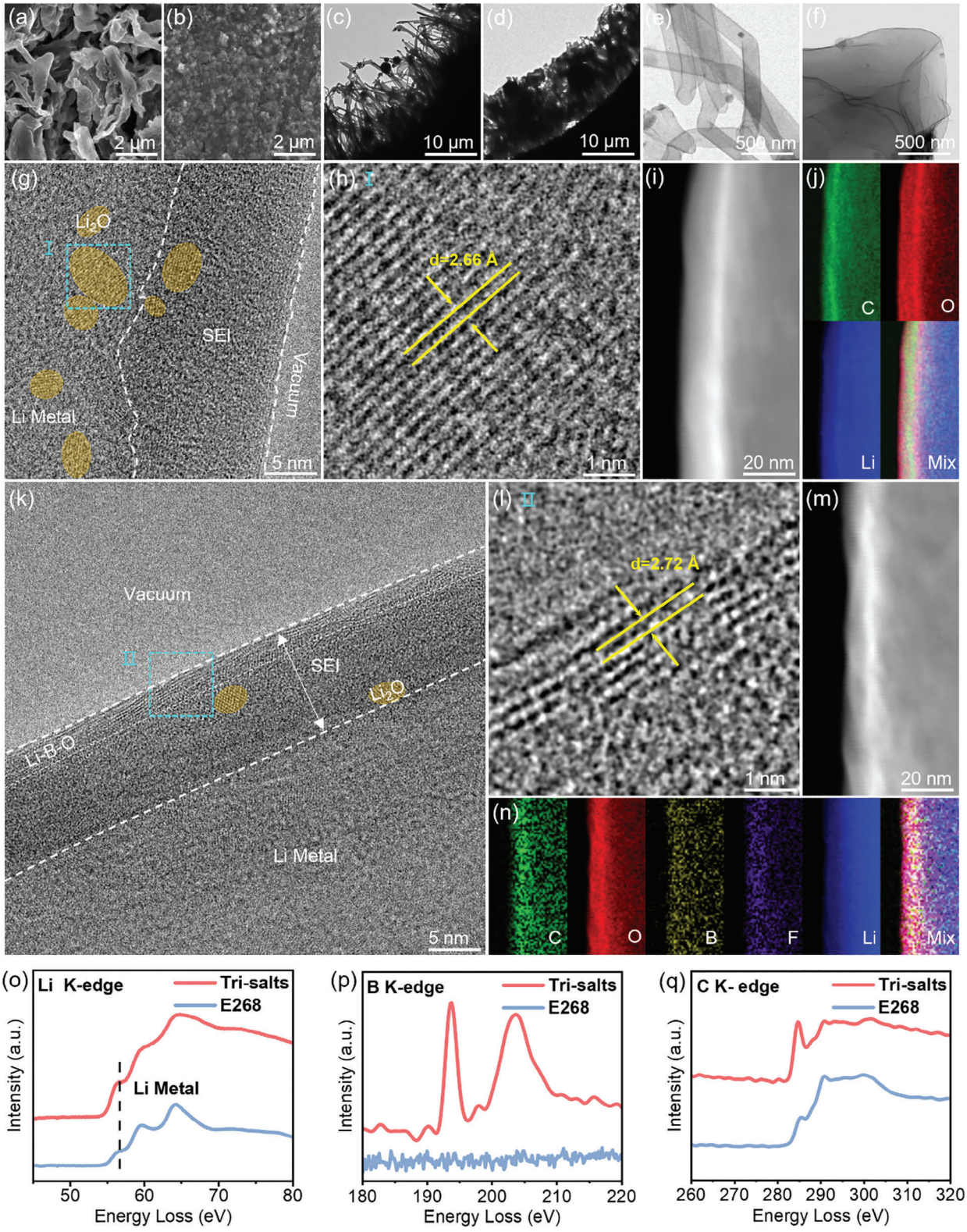

Figure 3. a–f) Li plating/stripping performance in different electrolytes. a,b) Top-view SEM images of deposited Li-metal anodes in NMC83||Li after 100 cycles in a) E268 and b) Tri-salts. c–f) STEM image in c,e) E268 and d,f) Tri-salts. g–n) Cryo-TEM image of Li deposited on a TEM grid and EELS elemental mapping results magnified view of selected area of g–j) E268 and k–n) Tri-salts. o–q) EELS spectra of o) Li, p) B, and q) C K-edge.

A borate-rich SEI layer was constructed in the Tri-salts electrolyte, which is not observed in E268. The spectra shown in Figure 3o indicate that there is a passivation plateau in the Li K-edge spectrum of the Tri-salts electrolyte, which may be caused by the mixed valence states of Li_2O and LiF in the SEI.[43] The signal of B originates from $LiBF_4$ and LiDFOB (Figure 3p and Figure S11, Supporting Information), and the double peaks of B in the spectral signals at 193.7 and 203.6 eV are similar to those of the standard spectra provided in literature for the two substances Li_3BO_3 and $Li_4B_2O_5$ which are closest to the two substances provided in the literatures.[44,45] This further suggests that a continuous and dense borate-based bilayer SEI was formed. The C K-edge peaks at 285 and 290 eV correspond to the Π*(C—C) and Π*(O—C═O) bonds (Figure 3q and Figure S11, Supporting Information).

To further explore the composition of the SEI, we performed X-ray photoelectron spectroscopy (XPS) analysis on the lithium metal electrodes after 100 cycles. The signal of C—C/C—H and C—O groups in E268 were much more intense than those in Tri-salts (**Figure** 4a,e), indicating that more organic compounds were produced in E268.[46,47] The higher organic component ratios imply a lower mechanical strength of the SEI films which will facilitate the Li-metallic dendrite growth. Noted that in O 1s spectra (Figure 4b,f and Figure S12, Supporting Information), the binding energy intense between transition metal and oxygen (M—O) in Tri-salts is much stronger than that in the other three electrolytes. The content of M—O was generally employed as an indicator of SEI thickness.[30,48] In this regard, we observed that the SEI formed in the Tri-salts electrolyte was comparatively thinner than that produced in E268, which aligns with the findings obtained from Cryo-TEM imagines. The F 1s spectra (Figure 4c) revealed that the SEI produced in the Tri-salts electrolytes featured a content of B—F specie which could originate from decomposition of the LiDFOB and $LiBF_4$ additives. The appearance of B—O and B—F signal peaks at 191.7 and 192.7 eV further suggests that B is involved in the formation of SEI in the Tri-salts electrolyte (Figure 4d).

Figure 4g,h shows the quantification result of cell capacity loss,[30] which can be used to investigate SEI dissolution in the real cases with electrolytes.[49] Li||Cu cells with 70 µL electrolytes were cycled in the voltage range of 0.005–2 V, pausing at 2 V for x h after every 5 cycles (x = 50, 30, 15 and 5) to investigate SEI dissolution. Clearly, the capacities in Tri-salts electrolyte are higher than that in the E268 electrolyte, and the capacity increment after each pause indicates the parasitic reduction reactions of electrolyte decomposition (Figure 4g). The capacity loss following a pause of x hours (difference of capacity after and before each pause) can be used to quantify the dissolution of SEI in each electrolyte (Figure 4h).[50] It is evident that the average capacity loss after a 50 h pause for E268 (3.23 µAh) is 3.36 times higher than that of the Tri-salts electrolyte (0.96 µAh). Clearly, compared to the E268 electrolyte, the Tri-salts electrolyte provides a more stable working environment for lithium metal anode.

2.4. Mechanism Discussion for the Enhanced Performance

We hypothesize that the excellent properties of the bilayer SEI are due to the effect of borates deposited in the bulk of the surface layer. To gain a comprehensive understanding of the underlying factors contributing to the enhanced electrochemical performance, density-functional theory (DFT) calculations were performed. The migration barrier energies and adsorption energy barriers of Li ions on the $LiBO_2$, Li_2O, and LiF were calculated and compared (**Figure** 5a–d). The migration barrier energy for the Li atom in the migration (001) path on the $LiBO_2$ crystal is found to be 0.37 eV. However, the migration barriers of Li atoms on the (111) plane of Li_2O and (001) plane of LiF are determined to be 0.22 and 0.13 eV, respectively. These calculations suggest that compared to Li_2O and LiF, there are higher migration barriers for Li atoms on the crystal planes of $LiBO_2$ (Figure 5a–c). Moreover, the adsorption energy of Li atoms on $LiBO_2$ is lower than that in Li_2O and LiF (Figure 5d). It is well known that the adsorption and diffusion energy barrier is of great significance for the study of SEI,[51,52] and a larger adsorption energy implies a stronger affinity, which can effectively reduce the nucleation barrier and decrease the polarization. And the faster the Li-ion diffusion kinetics, the more benefit it is to promote the uniform lateral diffusion of Li-ion flow, thus avoiding dendrite generation. Hence, the presence of the fabricated borate-based bilayer SEI appears to be detrimental to achieving uniform lithium deposition and suppressing dendrite formation.

However, considering the electrochemical performance and surface morphology of the anode, we propose that the continuous and dense formation of inorganic components during the SEI formation process plays a decisive role in the lithium-ion deposition behaviors. Although $LiBO_2$ does not have excellent adsorption and diffusion barriers, it performs a continuous and complete structure on the SEI surface, thereby exhibiting outstanding performance in inhibiting dendritic crystal growth and promoting homogeneous deposition, and improving cycling performance of the high energy density LMBs. Hence, based on the above understanding, the design of electrolyte structure and component screening should prioritize the in situ formation of continuous and compact inorganic constituents within the SEI layer.

3. Conclusion

In this work, we have developed a concentrated Tri-salts electrolyte that effectively supports the long-term stability of LMBs with high NMC83 mass-loading. The capacity retention of Li||NMC83 was 94.49% after 100 cycles at 0.33C/0.33C and 89.89% after 200 cycles at 0.1C/0.33C. Experiments and theoretical calculations confirm that the enhanced cycle stability of LMBs by the designed Tri-salts electrolyte is primary attributed to the continuous and dense borate-based inorganic SEI layer, which inhibits the growth of lithium dendrites and promotes uniform lithium deposition. Furthermore, the designed Tri-salts electrolyte exhibits flame retardancy, presenting great potential for the safety of LMBs. The correlation between the refined SEI structures and improved stability is highly meaningful for researchers in this field to formulate rational principles of electrolyte engineering.

4. Experimental Section

Preparation of Electrode and Electrolyte: Electrolyte Preparation: The carbonate-based electrolyte consisting of 1 M $LiPF_6$ in ethyl carbonate

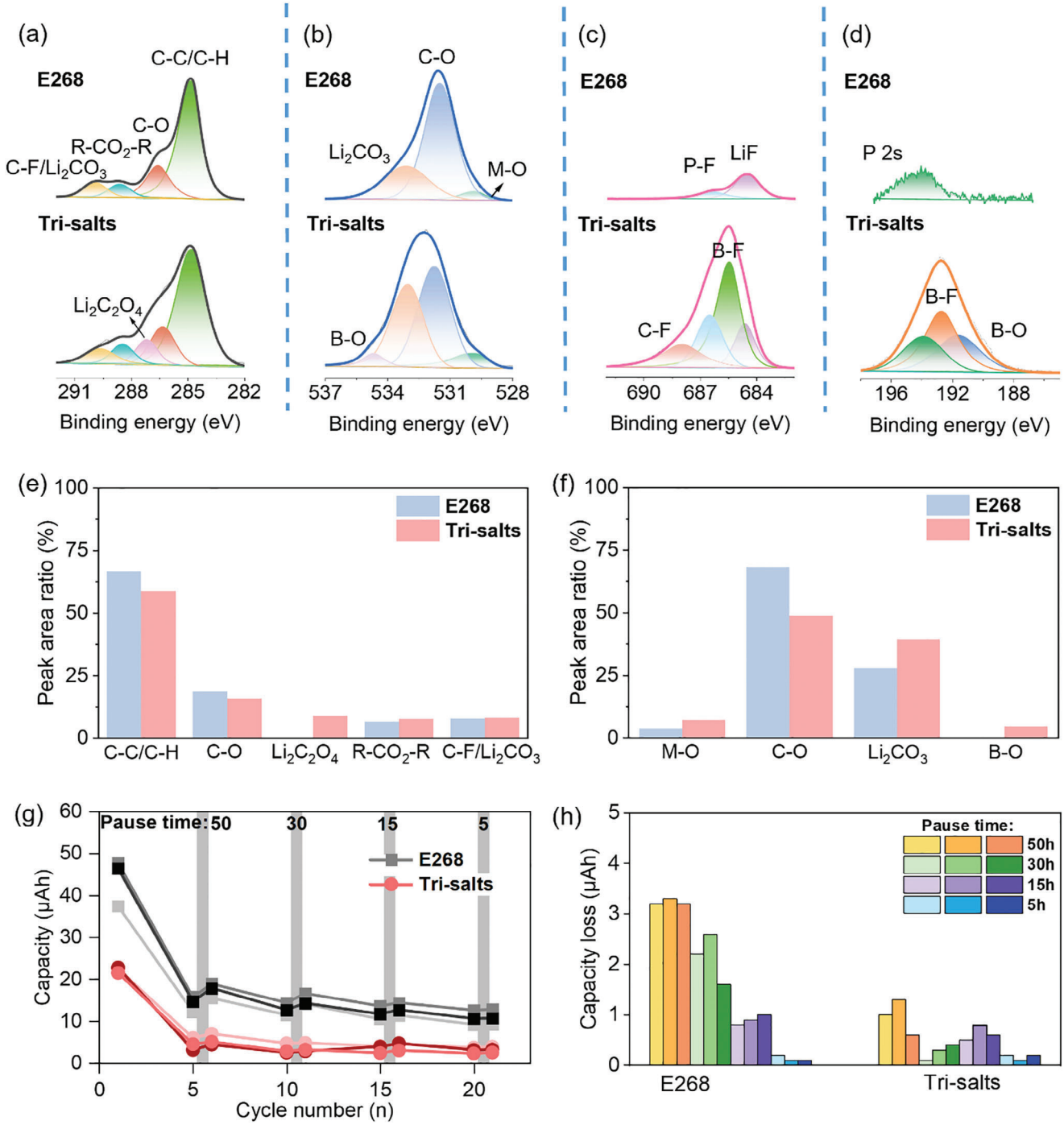

Figure 4. SEI films formed and dissolution analyzed. a–d) XPS spectra of the SEI films formed on Li-metal anodes in different electrolytes. e,f) The ratios of different species in e) C 1s and f) O 1s spectrum. g) The capacity from the reduction reaction of electrolytes before and after each pause time as a function of cycle numbers. The gray area with arbitrary width means cell pause processes. h) The capacity loss for different pause times in E268 and Tri-salts. Each shade of color represents a cell.

(EC)/ethyl methyl carbonate (EMC) 3:7 with 2 wt% vinylidene carbonate (VC) (denoted as E268), 1.5 M $LiPF_6$ and 1 M $LiBF_4$ in dimethyl carbonate (DMC)/EC / EMC 14:5:1 in wt% (denoted as Dual-salts-1), 1.5 M $LiPF_6$ and 1.5 M LiDFOB in DMC/EC/EMC 14:5:1 in wt% (denoted as Dual-salts-2) were used as reference. 1.5 M $LiPF_6$, 1 M $LiBF_4$, and 1.5 M LiDFOB in DMC/ EC/ EMC 14:5:1 in wt% is prepared, labeled as Tri-salts electrolyte. All the salts and solvents were purchased from Aladdin.

Electrode Preparation: $LiNi_{0.83}Co_{0.12}Mn_{0.05}O_2$ (NMC83), polyvinylidene fluoride (PVDF), and acetylene black (94:3:3 in weight) were first mixed and dissolved in N-methyl-2-pyrrolidone (NMP) solvent. Then, the prepared slurry was coated on aluminum foil, vacuum-dried at 80 °C for

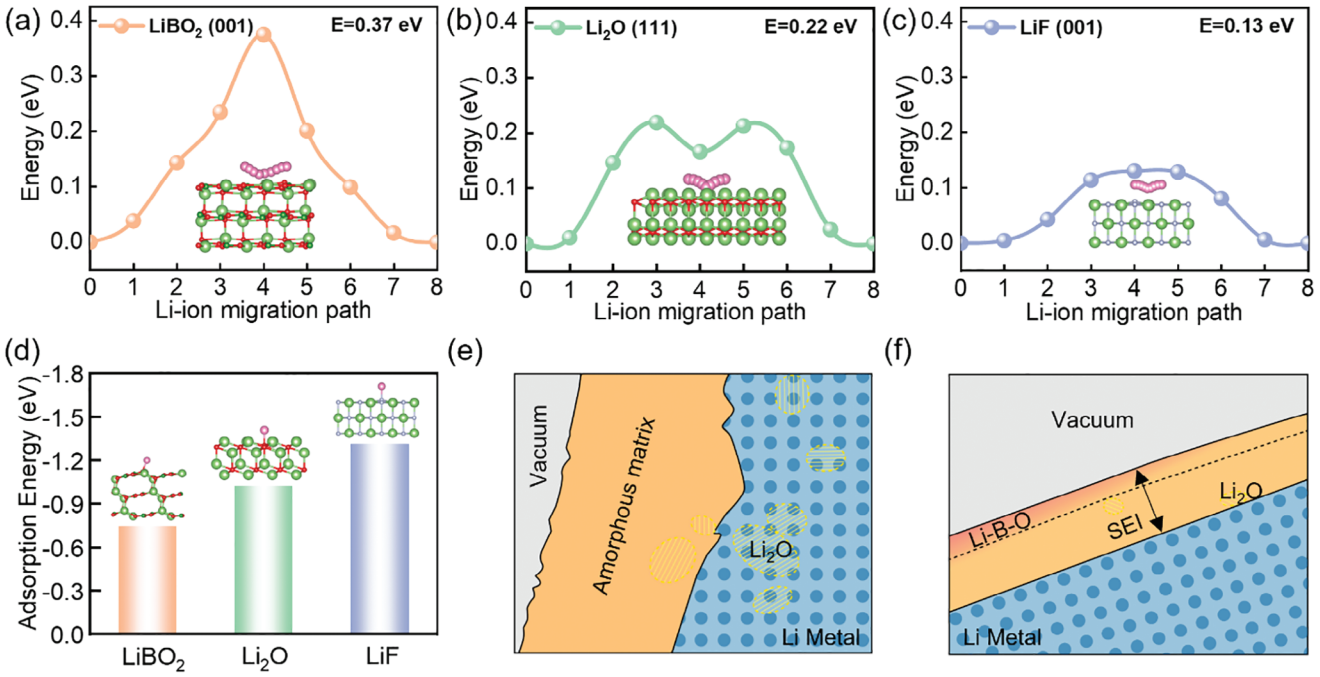

Figure 5. a–c) The migration path and kinetic energy barrier of Li^+ on a) $LiBO_2$ (001), b) Li_2O (111), and c) LiF (001) surfaces. d) Adsorption energy for $LiBO_2$, Li_2O and LiF. e,f) Schematic of the observed SEI structure on deposited Li in e) E268 and f) Tri-salts.

12 h, and followed by 110 °C for 12 h. The electrode was finally cut into 1.33 cm^{-2} disks to prepare NMC83 electrodes. The areal mass-loading of the NMC83 is about 20 mg cm^{-2}. Battery-grade lithium foil's diameter is 15.6 mm, and its thickness is 450 µm.

Electrochemical Performance Measurements: The stability of electrolytes with various compositions were tested by LSV measurements on an electrochemical workstation at a scan rate of 1 mV s^{-1} (Chi660e, China). Long-term cycling tests were conducted on a battery analyzer (Lanhe, Wuhan Land Co., Ltd). Three activation cycles were first conducted at 0.1 C before charge/discharge cycling at 0.33 C and charge at 0.1 C/discharge at 0.33 C between 4.5–2.7 V under 25 °C and 45 °C. Li||Li cells were cycled at 1 mA cm^{-2} for 1 h, and the Cu||Li cells were performed at 1.58 mA between 0 and 1 V. The ionic conductivities of electrolytes were measured through assembling symmetric stainless-steel cells. The electrolytic conductivity value was obtained from the impedance spectroscopy of the customized two-electrode cell by the following equation:

$$\delta = L/A \times R \tag{1}$$

where R is the ohmic resistance, A is the area, and L is the space between two stainless steel electrodes, respectively. The EIS tests were performed in the frequency range of 100 000 Hz to 0.01 Hz with an amplitude of 10 mV. To investigate the effect of SEI dissolution, Li||Cu cells with 75 µL electrolytes were cycled in the voltage range of 0.005–2 V to form the SEI layer on the Cu surface and paused at the 2 V state for x h (x = 50, 30, 15 and 5) after every 5 cycles to illustrate SEI dissolution.

Characterization: The morphologies and microstructures of the samples were characterized by scanning electron microscopy (SEM, JSM 7800F, JEOL). Cryogenic TEM (Titan Krios) images were acquired at 77 K using a Falcon 3 camera, and a low does condition 7–10 e $Å^{-2}$ s^{-1} × 10 s at a counting model for high-resolution TEM imaging) was applied. The TEM specimen was prepared via placing a Cu grid on the bare Cu foil. After Li deposition, the half-cell was disassembled in an Ar-filled glovebox, washed with DMC, dried at 60 °C, placed in a vacuum chamber and transferred to Cryo-TEM center, where the Cu grids were cooled with liquid nitrogen and mounted onto a Cryo-transfer sample holder of the Cryo-TEM. The beam electron metrology rate is strictly controlled during the acquirement of images and the electron energy loss spectrum (EELS). The chemical components of the samples were determined by X-ray photoelectron spectroscopy (XPS, K-Alpha+, Thermo Fisher Scientific). Raman spectra were recorded by using a Renishaw in Via Raman microscope with λ = 532 nm laser radiation.

Theoretical Calculations: The calculations of Li-ion behaviors on the surface were carried out by using spin-polarized DFT with the generalized gradient approximation (GGA) and Perdew-Burke-Ernzerhof (PBE) as implemented in the Vienna ab initio simulation package (VASP).[53] The plane-wave energy cutoff was set to 520 eV for all calculations. The convergence threshold was set at 10^{-5} eV for the iteration in self-consistent field (SCF) and 0.02 eV $Å^{-1}$ for maximum force component. The van der Waals interactions were described using the empirical correction in DFT-D3. The supercell sizes were set to $2\sqrt{2}\times2\sqrt{2}\times2$, 1×2×2, 1×2×3 for LiF (001), Li_2O (111) and $LiBO_2$ (001) slab model, respectively. We utilized a 3×3×1 Monkhorst-Pack k-point mesh for the LiF (001), Li_2O (111) and $LiBO_2$ (001) surface diffusions, respectively. To avoid interaction artificial between neighboring images, a vacuum spacing of more than 25 Å was introduced in the surface diffusion calculations. The climbing image-nudged elastic band (CI-NEB) method[54] was employed to determine the energy barrier of the Li ion diffusion. The adsorption energies (Eads) were calculated as follows:

$$E_{ads} = E_{slab-ads} - E_{slab} - E_{ads} \tag{2}$$

where $E_{slab\text{-}ads}$ is the total energy for the absorbed surface of a species, E_{slab} the SEI surface and E_{ads} Li ions.

MD simulations were performed in GROMACS using the General Amber Force Field (GAFF) parameters. Topology files and bonded and Lennard-Jones parameters were generated by using the Autoff while the RESP atomic charges from Multiwfn3.8 program were used.[55] The cutoff for the Lennard-Jones potential was set to 12 Å. The long-range Coulombic interactions were counted by a particle–particle particle-mesh. The initial periodic systems were set up using PACKMOL.[56] All ions and molecules were inserted in an initial cube box with 10 nm sides. In the equilibrium

stage of the system, the energy of the simulated system was minimized by the conjugate gradient method first, then the equilibrium simulation was carried out under NPT ensemble for 10 ns. Finally, the simulation was continued for 20 ns with NVT ensemble and data were collected. Only the final 10-ns trajectory was sampled for the analysis of radial distribution function and solvent-solute interaction environments.

Supporting Information

Supporting Information is available from the Wiley Online Library or from the author.

Acknowledgements

This work was financially backed by National Natural Science Foundation (NNSF) of China (No. 52202269, 52002248). Additionally, the authors received support from the Shenzhen Science and Technology program (No. 20220810155330003), Shenzhen Science and Technology Program (NO. KJZD20230923115005009), Project of Department of Education of Guangdong Province (No. 2022ZDZX3018), and Xiangjiang Lab (22XJ01007). The authors thank to the Major Science and Technology Infrastructure Project of Material Genome Big-science Facilities Platform supported by Municipal Development and Reform Commission of Shenzhen, and Instrumental Analysis Center at Shenzhen University's Xili Campus for supplying the necessary facilities for the material analysis.

Conflict of Interest

The authors declare no conflict of interest.

Author Contributions

Y.L.: conceptualization, methodology, experiments, formal analysis, characterization of samples, writing–original draft. T.H.: formal analysis. Z.H.: formal analysis. W.H.: investigation. J.C.: investigation. H.J.: investigation. X.H. visualization. W.C.: visualization. H.W.: visualization. L.L.: investigation. X.R.: investigation. X.O.: supervision, investigation. J.L.: supervision, investigation. S.Y.: investigation. X.Y.: visualization, writing–review & editing. Q.Z.: supervision, project administration, writing–review & editing. F.P.: project administration, writing–review & editing. J.H.: supervision, project administration, writing–review & editing.

Data Availability Statement

The data that support the findings of this study are available from the corresponding author upon reasonable request.

Keywords

borate-based bilayer SEI, electrolytes, lithium metal batteries, uniform deposition

Received: July 27, 2024
Revised: October 17, 2024
Published online:

[1] M. Winter, B. Barnett, K. Xu, *Chem. Rev.* **2018**, *118*, 11433.
[2] J. M. Tarascon, M. Armand, *Nature* **2001**, *414*, 359.
[3] W. J. Zhang, *J. Power Sources* **2011**, *196*, 13.
[4] D. C. Lin, Y. Y. Liu, Y. Cui, *Nat. Nanotechnol.* **2017**, *12*, 194.
[5] K. Brandt, *Solid State Ionics* **1994**, *69*, 173.
[6] M. S. Whittingham, *Chem. Rev.* **2004**, *104*, 4271.
[7] X. Q. Zhang, X. Chen, X. B. Cheng, B. Q. Li, X. Shen, C. Yan, J. Q. Huang, Q. Zhang, *Angew. Chem., Int. Ed.* **2018**, *57*, 5301.
[8] Y. L. Jie, X. D. Ren, R. G. Cao, W. B. Cai, S. H. Jiao, *Adv. Funct. Mater.* **2020**, *30*, 1910777.
[9] C. W. Wang, K. Fu, S. P. Kammampata, D. W. McOwen, A. J. Samson, L. Zhang, G. T. Hitz, A. M. Nolan, E. D. Wachsman, Y. F. Mo, V. Thangadurai, L. B. Hu, *Chem. Rev.* **2020**, *120*, 4257.
[10] Z. B. Xu, Y. R. Yu, Y. Y. Huang, Z. Y. Huang, P. Li, G. Liu, Z. Wang, *J. Power Sources* **2023**, *579*, 233274.
[11] C. Wu, F. H. Guo, L. Zhuang, X. P. Ai, F. P. Zhong, H. X. Yang, J. F. Qian, *ACS Energy Lett.* **2020**, *5*, 1644.
[12] R. Zhang, N. W. Li, X. B. Cheng, Y. X. Yin, Q. Zhang, Y. G. Guo, *Adv. Sci.* **2017**, *4*, 1600445.
[13] F. H. Guo, C. Wu, S. L. Chen, X. P. Ai, F. P. Zhong, H. X. Yang, J. F. Qian, *ACS Mater. Lett.* **2020**, *2*, 358.
[14] S. Li, M. W. Jiang, Y. Xie, H. Xu, J. Y. Jia, J. Li, *Adv. Mater.* **2018**, *30*, 1706375.
[15] S. R. Chen, J. M. Zheng, D. H. Mei, K. S. Han, M. H. Engelhard, W. G. Zhao, W. Xu, J. Liu, J. G. Zhang, *Adv. Mater.* **2018**, *30*, 1706375.
[16] X. Cao, X. D. Ren, L. F. Zou, M. H. Engelhard, W. Huang, H. S. Wang, B. E. Matthews, H. Lee, C. J. Niu, B. W. Arey, Y. Cui, C. M. Wang, J. Xiao, J. Liu, W. Xu, J. G. Zhang, *Nat. Energy* **2019**, *4*, 796.
[17] X. Cao, H. Jia, W. Xu, J. G. Zhang, *J. Electrochem. Soc.* **2021**, *168*, 1706375.
[18] J. Zheng, G. B. Ji, X. L. Fan, J. Chen, Q. Li, H. Y. Wang, Y. Yang, K. C. DeMella, S. R. Raghavan, C. S. Wang, *Adv. Energy Mater.* **2019**, *9*, 1706375.
[19] X. L. Fan, X. Ji, L. Chen, J. Chen, T. Deng, F. D. Han, J. Yue, N. Piao, R. X. Wang, X. Q. Zhou, X. Z. Xiao, L. X. Chen, C. S. Wang, *Nat. Energy* **2019**, *4*, 882.
[20] L. M. Suo, W. J. Xue, M. Gobet, S. G. Greenbaum, C. Wang, Y. M. Chen, W. L. Yang, Y. X. Li, J. Li, *Proc. Natl. Acad. Sci. USA* **2018**, *115*, 1156.
[21] L. M. Suo, O. Borodin, T. Gao, M. Olguin, J. Ho, X. L. Fan, C. Luo, C. S. Wang, K. Xu, *Science* **2015**, *350*, 938.
[22] Q. F. Zheng, Y. Yamada, R. Shang, S. Ko, Y. Y. Lee, K. Kim, E. Nakamura, A. Yamada, *Nat. Energy* **2020**, *5*, 291.
[23] D. W. McOwen, D. M. Seo, O. Borodin, J. Vatamanu, P. D. Boyle, W. A. Henderson, *Energy Environ. Sci.* **2014**, *7*, 416.
[24] K. Matsumoto, K. Inoue, K. Nakahara, R. Yuge, T. Noguchi, K. Utsugi, *J. Power Sources* **2013**, *231*, 234.
[25] A. J. Louli, A. Eldesoky, R. Weber, M. Genovese, M. Coon, J. deGooyer, Z. Deng, R. T. White, J. Lee, T. Rodgers, R. Petibon, S. Hy, S. J. H. Cheng, J. R. Dahn, *Nat. Energy* **2020**, *5*, 693.
[26] J. H. Wang, Y. Yamada, K. Sodeyama, E. Watanabe, K. Takada, Y. Tateyama, A. Yamada, *Nat. Energy* **2018**, *3*, 22.
[27] W. Wang, J. L. Zhang, Q. Yang, S. W. Wang, W. H. Wang, B. H. Li, *ACS Appl. Mater.* **2020**, *12*, 22901.
[28] H. Zheng, H. F. Xiang, F. Y. Jiang, Y. C. Liu, Y. Sun, X. Liang, Y. Z. Feng, Y. Yu, *Adv. Energy Mater.* **2020**, *10*, 1706375.
[29] H. Su, Z. Chen, M. Li, P. Bai, Y. Li, X. Ji, Z. Liu, J. Sun, J. Ding, M. Yang, X. Yao, C. Mao, Y. Xu, *Adv. Mater.* **2023**, *35*, 2301171.
[30] Q. Y. Dong, F. Guo, Z. J. Cheng, Y. Y. Mao, R. Huang, F. S. Li, H. C. Dong, Q. Y. Zhang, W. Li, H. Chen, Z. J. Luo, Y. B. Shen, X. D. Wu, L. W. Chen, *ACS Appl. Energy Mater.* **2020**, *3*, 695.
[31] X. F. Bian, S. X. Ge, Q. Pang, K. Zhu, Y. J. Wei, B. Zou, F. Du, D. Zhang, G. Chen, *J. Alloys Compd.* **2018**, *736*, 136.
[32] L. S. Su, K. Jarvis, H. Charalambous, A. Dolocan, A. Manthiram, *Adv. Funct. Mater.* **2023**, *33*, 2213675.
[33] F. H. Ren, Z. D. Li, J. H. Chen, P. Huguet, Z. Peng, S. Deabate, *ACS Appl. Mater.* **2022**, *14*, 4211.

[34] X. Y. Zheng, Z. Y. Gu, J. Fu, H. T. Wang, X. L. Ye, L. Q. Huang, X. Y. Liu, X. L. Wu, W. Luo, Y. H. Huang, *Energy Environ. Sci.* **2021**, *14*, 4936.
[35] L. S. Su, X. H. Zhao, M. Yi, H. Charalambous, H. Celio, Y. Y. Liu, A. Manthiram, *Adv. Energy Mater.* **2022**, *12*, 2201911.
[36] Z. Cao, X. Y. Zheng, Q. T. Qu, Y. H. Huang, H. H. Zheng, *Adv. Mater.* **2021**, *33*, 2201911.
[37] K. Xu, M. S. Ding, S. S. Zhang, J. L. Allen, T. R. Jow, *J. Electrochem. Soc.* **2002**, *149*, A622.
[38] S. Y. Chen, Z. X. Wang, H. L. Zhao, H. W. Qiao, H. L. Luan, L. Q. Chen, *J. Power Sources* **2009**, *187*, 229.
[39] H. Chen, B. Liu, Y. Wang, H. Guan, H. Zhou, *J. Alloys Compd.* **2021**, *876*, 159966.
[40] Y. Z. Li, Y. B. Li, A. L. Pei, K. Yan, Y. M. Sun, C. L. Wu, L. M. Joubert, R. Chin, A. L. Koh, Y. Yu, J. Perrino, B. Butz, S. Chu, Y. Cui, *Science* **2017**, *358*, 506.
[41] M. Chen, J. H. Zheng, Y. J. Liu, O. W. Sheng, Z. J. Ju, G. X. Lu, T. F. Liu, Y. Wang, J. W. Nai, Q. Wang, X. Y. Tao, *Adv. Funct. Mater.* **2021**, *31*, 2102228.
[42] Z. W. Zhang, Y. Z. Li, R. Xu, W. J. Zhou, Y. B. Li, S. T. Oyakhire, Y. C. Wu, J. W. Xu, H. S. Wang, Z. A. Yu, D. T. Boyle, W. Huang, Y. S. Ye, H. Chen, J. Y. Wan, Z. N. Bao, W. Chiu, Y. Cui, *Science* **2022**, *375*, 66.
[43] X. Z. Lu, Y. F. Cheng, M. H. Li, Y. C. Zou, C. Zhen, D. J. Wu, X. B. Wei, X. Y. Li, X. M. Yang, M. Gu, *Adv. Funct. Mater.* **2023**, *33*, 2212847.
[44] G. Lelong, L. Cormier, L. Hennet, F. Michel, J.-P. Rueff, J. M. Ablett, G. Monaco, *J. Non-Cryst. Solids* **2017**, *472*, 1.
[45] P. S. Miedema, P. Ngene, A. M. J. van der Eerden, D. Sokaras, T. C. Weng, D. Nordlund, Y. S. Au, F. M. F. de Groot, *Phys. Chem. Chem. Phys.* **2014**, *16*, 22651.
[46] C. C. Su, M. N. He, R. Amine, Z. H. Chen, R. Sahore, N. D. Rago, K. Amine, *Energy Storage Mater.* **2019**, *17*, 284.
[47] X. S. Wang, S. W. Wang, H. R. Wang, W. Q. Tu, Y. Zhao, S. Li, Q. Liu, J. R. Wu, Y. Z. Fu, C. P. Han, F. Y. Kang, B. H. Li, *Adv. Mater.* **2021**, *33*, 2007945.
[48] B. Li, Y. X. Shao, J. J. He, R. C. Chen, S. X. Huang, Z. L. Wu, J. H. Li, Z. S. Wang, G. C. Liu, *Electrochim. Acta* **2022**, *426*, 140783.
[49] L. A. Ma, A. J. Naylor, L. Nyholm, R. Younesi, *Angew. Chem., Int. Ed.* **2021**, *60*, 4855.
[50] Y. Jin, P. M. L. Le, P. Y. Gao, Y. B. Xu, B. W. Xiao, M. H. Engelhard, X. Cao, T. D. Vo, J. T. Hu, L. R. Zhong, B. E. Matthews, R. Yi, C. M. Wang, X. L. Li, J. Liu, J. G. Zhang, *Nat. Energy* **2022**, *7*, 718.
[51] J. L. Jiang, X. F. Hu, S. Y. Lu, C. Shen, S. S. Huang, X. Y. Liu, Y. Jiang, J. J. Zhang, B. Zhao, *Energy Storage Mater.* **2023**, *54*, 885.
[52] Y. N. Li, A. J. Hu, X. D. Gan, M. He, J. Zhu, W. Chen, Y. Hu, T. Y. Lei, F. Li, Y. Y. Li, Y. X. Fan, F. Wang, M. J. Zhou, A. Wen, B. H. Li, *Nano Res.* **2023**, *16*, 8304.
[53] G. Kresse, J. Furthmuller, *Comput. Mater. Sci.* **1996**, *6*, 15.
[54] G. Henkelman, B. P. Uberuaga, H. Jónsson, *J. Chem. Phys.* **2000**, *113*, 9901.
[55] T. Lu, F. W. Chen, *J. Comput. Chem.* **2012**, *33*, 580.
[56] L. Martínez, R. Andrade, E. G. Birgin, J. M. Martínez, *J. Comput. Chem.* **2009**, *30*, 2157.